Journal of Materials Chemistry A

ROYAL SOCIETY OF CHEMISTRY

PAPER

View Article Online
View Journal

Cite this: DOI: 10.1039/d5ta09128d

Interfacial pathways in $Na_2B_{12}H_{12}/SiO_2$ nanocomposites boost the ionic conductivity and enable solid-state sodium batteries at room temperature

Jonas D. Hehn, [a] Gabriele Masia,[ab] Masoud Lazemi, [a] Juliette C. Verschoor,[a] Karan Kotalgi,[a] Savannah J. Turner, [c] Hlynur Gretarsson,[d] Martin Sundermann, [de] Fabrizio Murgia,[b] Petra E. de Jongh [a] and Peter Ngene *[a]

All-solid-state sodium metal batteries are an attractive alternative to Li-ion batteries due to their high energy density, improved safety, and the lower price of sodium. A major bottleneck is the development of suitable solid electrolytes with sufficient ionic conductivity and electrochemical stability. Here, we report new all-solid-state sodium metal batteries based on sodium *closo*-dodecahydridoborate ($Na_2B_{12}H_{12}$) electrolyte and both Prussian white ($Na_2MnFe(CN)_6$) and TiS_2 cathode active materials. Although the pristine $Na_2B_{12}H_{12}$ has a low ionic conductivity at room temperature, the conductivity increases by more than three orders of magnitude upon nanocomposite formation with mesoporous SiO_2 *via* high-energy ball milling. The high ionic conductivity (5×10^{-4} S cm^{-1}, 30 °C) and oxidative stability (3.9 V *vs.* Na^+/Na) of $Na_2B_{12}H_{12}/SiO_2$ enable room-temperature battery operation with impressive capacity retention. Using a variety of techniques, including X-ray Raman scattering and electron energy loss spectroscopy, we show the presence of an interphase formed by an interface reaction between $Na_2B_{12}H_{12}$ and SiO_2. The observed interface effects are highly influenced by the morphology of the oxidic framework and the preparation conditions of the nanocomposite.

Received 10th November 2025
Accepted 6th February 2026

DOI: 10.1039/d5ta09128d

rsc.li/materials-a

Introduction

Sustainable energy production relies on fluctuating factors such as sunshine or wind; therefore, reliable and secure solutions are essential for storing the generated electrical energy. The lithium-ion (Li-ion) battery technology is paving the way to address this global energy challenge.[1] On the other hand, battery technologies based on geographically widespread, abundant and potentially cheaper elements offer attractive development prospects. Hence, sodium-ion (Na-ion) based battery chemistries are a promising alternative to Li-ion batteries.[2,3] Although the high energy densities of state-of-the-art Li-ion batteries remain unchallenged, next-generation sodium batteries, such as those utilizing solid electrolytes (SEs), are a promising option. Certain SEs are compatible with metallic anodes, enabling capacities beyond the limits of commercially used anodes.[4,5] Additionally, the replacement of the flammable liquid electrolytes with SEs would potentially improve the safety aspects of sodium batteries.[5]

These promising features have led to enormous efforts in the scientific community to develop new SEs. Next to sodium superionic conductors (NASICON),[6,7] β-alumina[7,8] and sulfide-based[7,9] solid-state Na-ion conductors, sodium hydridoborates have recently gained particular interest.[10,11] Due to their good mechanical properties (softness) and superior reductive stability, excellent interface contact can be established with different classes of electrodes, including sodium metal anodes (Na metal).[12] One example of this class of materials is $Na_2B_{12}H_{12}$, which is non-flammable and has a low density (hence high energy content), due to its composition of only light elements.[13–16] Following a temperature-induced polymorphic transition above 256 °C, ionic conductivities of ~0.1 S cm^{-1} were reported.[17,18] Approaches like nanostructuring[17,19,20] or partial anion substitution[21–23] aim to stabilize the high-temperature polymorph of these polyhedral-hydridoborate salts. Other strategies are the controlled oxidation[24–26] or the confinement in oxidic scaffold structures,[25,27,28] which leads to improved ionic conductivity potentially originating from the presence of boron oxygen bonds.

Building on these previous results, Su *et al.*[25] recently demonstrated that the mechanochemical treatment of oxidized

[a]*Materials Chemistry and Catalysis, Debye Institute for Nanomaterials Science, Utrecht University, 3584 CG Utrecht, The Netherlands. E-mail: p.ngene@uu.nl*
[b]*Department of Chemical, Physical, Mathematical and Natural Sciences, University of Sassari, 07100 Sassari, Italy*
[c]*Electron Microscopy Centre, Utrecht University, 3584 CG Utrecht, The Netherlands*
[d]*Deutsches Elektronen-Synchrotron DESY, 22607 Hamburg, Germany*
[e]*Max Planck Institute for Chemical Physics of Solids, 01187 Dresden, Germany*

$Na_2B_{12}H_{12}$ within a SiO_2 scaffold further enhances its electrochemical properties, similar to previous findings on related lithium hydridoborates.[29,30] This is interesting because various research groups[24,28] have earlier reported that nanocomposite formation with SiO_2 led to only a slight improvement in the ionic conductivity of sodium-based hydridoborates (*e.g.* $NaBH_4$), unlike in $Li_2B_{12}H_{12}$ and $LiBH_4$, for which enhancements in Li-ion conductivity were observed.[31–33] This raises the question whether the improved conductivity is primarily due to the partial oxidation of $Na_2B_{12}H_{12}$ or true interface effects.

Thus, in this work, we investigate the ionic conductivity and electrochemical properties of non-oxidized $Na_2B_{12}H_{12}/SiO_2$ nanocomposites, and the influence of the oxide scaffold properties on the conductivity of the nanocomposite. We used ordered mesoporous and pyrogenic SiO_2 with different surface-to-volume ratios to prepare $Na_2B_{12}H_{12}$-based nanocomposites. Using a variety of characterization techniques, we show that interface reaction with SiO_2 surface groups led to about four orders of magnitude increase in the Na-ion conductivity of the $Na_2B_{12}H_{12}$. We show that both the morphology of the SiO_2 and ball milling time have a profound impact on the overall ionic conductivity of the nanocomposite electrolytes. Furthermore, owing to the high stability window of the nanocomposite (3.9 V *vs.* Na^+/Na), we prepared an all-solid-state battery (ASSB) using a Na metal anode, and a high-voltage Prussian white (PW) cathode. The ASSB shows impressive capacity retention (>95%) after 50 cycles at room temperature (RT). This demonstrates the efficacy of interface engineering as a tool to tune the ionic conductivity and electrochemical properties of SEs.

Experimental section

Synthesis

$Na_2B_{12}H_{12}$ (>98%, KatChem) was dried at 200 °C for 16 h under reduced pressure (1 mbar) before use. Ordered mesoporous silica (SBA-15) or fumed SiO_2 (Aerosil 90, 200, 300, 380 from Degussa, Evonik) with distinct different Brunauer–Emmett–Teller (BET) surface areas (Table 1) were dried for 16 h at 270 °C under dynamic vacuum (1 mbar) and subsequently combined with $Na_2B_{12}H_{12}$. An overview of all sample compositions is provided in Table S1. All samples were handled and stored in an argon-filled glovebox (MBraun, Lab Star Glove Box, <1 ppm O_2 and <1 ppm H_2O). A Fritsch Pulverisette 7 ball mill with 20 mL tungsten carbide grinding bowls and 5 mm spheres was operated at 400 rpm to mechanochemically synthesize the nanocomposites in argon atmosphere. A discontinuous grinding process with 5-minute steps was performed, followed by a 5-minute break to prevent thermally induced decomposition. The ball-to-sample weight ratio was kept constant at 140 : 1, and an absolute amount of 500 mg per batch was used.

Structural characterization

Powder X-ray diffraction (XRD) patterns were recorded from $2\theta = 10°$ to 60° under argon atmosphere in an airtight low background specimen holder on a Bruker D2 Phaser with Cobalt $K_{\alpha 1,2}$ radiation, $\lambda = 1.79026$ Å (30 kV and 10 mA). A TriStar II Plus gas-volumetric instrument (Micromeritics) was used for nitrogen physisorption measurements at 77 K. The BET surface area was calculated by approximating a BET isotherm to the dataset ($0.05 < p/p_0 < 0.25$).[34] Diffuse reflectance infrared Fourier transform spectroscopy (DRIFTS) samples were diluted with 97 wt% KBr (≥99%, Sigma-Aldrich), ground to a fine powder, and measured in a moisture-free chamber compatible with the Praying Mantis system (Harrick Scientific Products) installed in a Nicolet iS50 FT-IR instrument (Thermo Fisher Scientific). X-ray Raman scattering (XRS) measurements were carried out using an airtight sample holder, described elsewhere[35] at beamline P01 of PETRA III, Deutsches Elektronen-Synchrotron (DESY), in Hamburg, Germany. Sample pellets were inserted into the holder and aligned at 18.3° with respect to the beam. Twelve spherically bent Si (220) analyzers centered around $2\theta = 55°$ focus the scattered photons onto a Medipix-3 pixel detector with a resolution of 0.7 eV. In the given geometry, XRS operates basically at the dipole limit, and the resulting spectra will be analogous to the X-ray absorption spectra (XAS).[30] The spectra were obtained by varying the incident beam energy while maintaining the analyzer energy fixed at about 9.7 keV. A Thermo Fisher Scientific Spectra 300 microscope was used for scanning transmission electron microscopy (STEM) at 300 kV combined with electron energy loss spectroscopy (EELS). Scanning electron microscopy (SEM) imaging was carried out on a Zeiss Evo 15 microscope operated at 15 kV. Elemental mapping was performed with energy dispersive X-ray spectroscopy (EDS).

Electrochemical characterization

A Parstat MC multichannel potentiostat with PMC-1000 module (AMETEK) was used for the electrochemical investigation of the nanocomposites. Potentiostatic electrochemical impedance spectroscopy (EIS) was performed by applying 10 mV AC from 1 MHz to 1 Hz. A typical EIS cell was assembled by compacting

Table 1 Morphological properties of various SiO_2 types

	Pore volume (ml g^{-1})	SiO_2 type	BET surface area (m^2 g^{-1})	Equivalent primary particle size
SiO_2-A90	152	Aerosil 90	70.2	85.5 nm
SiO_2-A200	437	Aerosil 200	191.2	31.4 nm
SiO_2-A300	742	Aerosil 300	271.5	22.1 nm
SiO_2-A380	692	Aerosil 380	349.2	17.2 nm
SiO_2-SBA15	1207	SBA-15	804.4	

40–50 mg of SE at 187 MPa between two rods ($A = 0.785$ cm^2), yielding pellets whose thickness ($L = 200$–400 μm) was obtained using a micrometer (Table S2).[30] The cathode composite used in the PW-ASSB cells was made from $Na_2MnFe(CN)_6$ (MSE PRO, theoretical capacity 171 mAh g^{-1}), SE and carbon (Ketjenblack EC600JD, AkzoNobel) in a 6 : 3 : 1 (RT cell) or 7 : 2.5 : 0.5 (40 °C cell) weight ratio. The PW cathode composites (RT cell: 1.5 mg, 0.541 mAh cm^{-2}; 40 °C cell: 1.2 mg, 0.505 mAh cm^{-2}) were uniaxially pressed with 347 MPa onto either a 35 mg (RT) or a 45 mg (40 °C) SE pellet with a theoretical thickness of 0.80 and 1.03 mm, respectively. If TiS_2 (99.9%, Sigma-Aldrich, theoretical capacity 239 mAh g^{-1}) was used as the cathode active material, it was blended in a 7 : 3 ratio with the SE. Subsequently, a freshly polished Na metal (99.9%, Sigma-Aldrich) disk and a copper current collector were added on the anode side. The three screws of the ASSB cells ($A = 0.283$ cm^2) were tightened to a torque of 1.2 Nm, which corresponds to a stack pressure of 106 MPa. Before applying a current, the ASSB cells were allowed to rest and equilibrate to the corresponding temperature for at least three hours at open circuit voltage.

Results and discussion

Effect of preparation conditions and oxide properties on the nanocomposite conductivity

A series of $Na_2B_{12}H_{12}/SiO_2$ nanocomposites with different compositions and mechanochemical treatment (ball milling) durations was prepared using SiO_2 scaffolds with different surface areas and morphologies in order to assess the effect of these parameters on the ionic conductivity. Fig. 1a compares the XRD patterns of the pristine $Na_2B_{12}H_{12}$ and SiO_2 with those of the nanocomposites ball milled for 4 h and 8 h. A clear change can be seen in the XRD pattern of the $Na_2B_{12}H_{12}$-phase after the mechanochemical treatment with SiO_2, whereby ball milling $Na_2B_{12}H_{12}$ in the absence of silica only reduces the crystallite size (Fig. S1a). The broadening of the main diffraction feature of $Na_2B_{12}H_{12}$ in the nanocomposite compared to the pristine material suggests that the mechanochemical treatment with varying SiO_2 content results in nanostructuring and some degree of amorphization of $Na_2B_{12}H_{12}$, as would be expected due to the mechanical impact (Fig. S1b).

As seen from Fig. 1b, the normalized intensity diffractogram of the nanocomposite ball-milled for 4 h shows broadening of the main peak at $2\theta = 17.6°$. This is due to the co-presence of the low-temperature monoclinic and the high-temperature $Na_2B_{12}H_{12}$ phases.[17,36] After an extended treatment duration of up to 8 h, a complete phase transformation of the monoclinic $Na_2B_{12}H_{12}$ phase is observed, as evidenced by the shift of the main diffraction peak at $2\theta = 17.6°$ to the slightly higher angle of $2\theta = 18.4°$ and the absence of a temperature-induced polymorphic transition (Fig. S2). These results demonstrate that mechanochemical treatment of $Na_2B_{12}H_{12}$ with SiO_2 leads to a loss of the long-range crystallinity and promotes the stabilization of the high-temperature $Pm\bar{3}n$ phase at RT, alongside the phases Pc and $P4_2/ncm$.

Fig. 2a compares the ionic conductivity of ball-milled $Na_2B_{12}H_{12}$ to that of nanocomposites containing 25 to 40 vol% SiO_2. The results show a profoundly higher ionic conductivity in the nanocomposites compared to that of nanostructured $Na_2B_{12}H_{12}$. Interestingly, the increase in conductivity largely depends on the amount of SiO_2, reaching a peak value (1.4×10^{-3} S cm^{-1} at 60 °C) at 35 vol% SiO_2, after which the conductivity decreases with increasing SiO_2 content. This demonstrates that nanocomposite formation with SiO_2 increases the ionic conductivity of $Na_2B_{12}H_{12}$ tremendously. Conversely, the decreased conductivity at high SiO_2 content is attributed to the absence of good percolation pathways for a facile transport of the Na-ions between the insulating SiO_2 particles.

Having established that nanocomposites made with 35 vol% SiO_2 are ideal for ion transport between the silica particles, hence show maximum ionic conductivity, the effect of ball

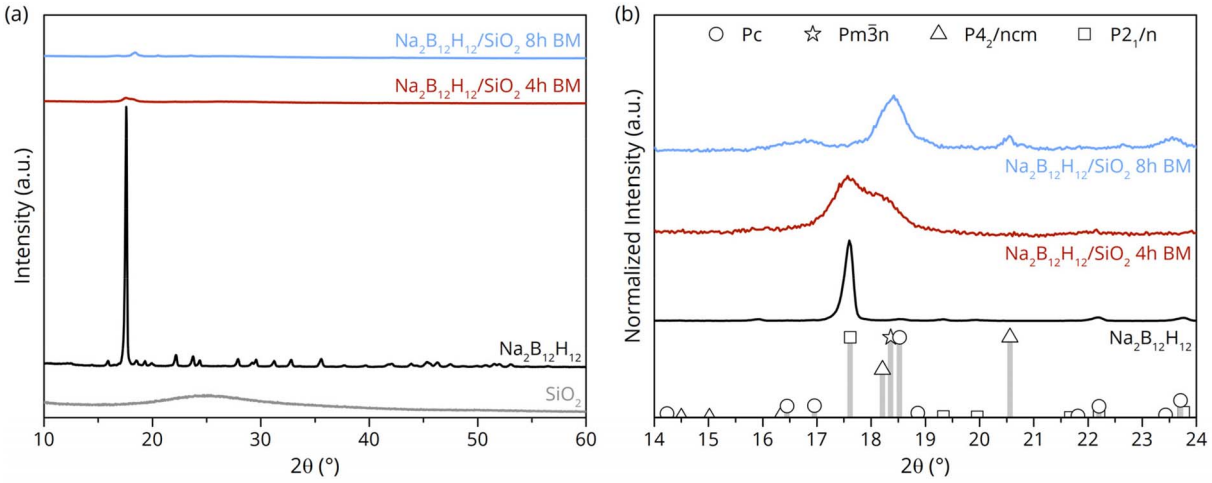

Fig. 1 (a) Room-temperature X-ray diffractograms for SiO_2, pristine $Na_2B_{12}H_{12}$ and $Na_2B_{12}H_{12}$/35 vol% SiO_2 nanocomposites ball-milled (BM) for 4 h and 8 h from 10°–60° 2θ. (b) Enlarged region highlighting the transition of the low temperature phase $P2_1/n$ (PDF 04-017-4134) upon ball milling; compared to $Na_2B_{12}H_{12}$ reference patterns Pc (PDF 04-023-3954), $Pm\bar{3}n$ (PDF 04-027-4286) and $P4_2/ncm$ (PDF 04-026-8454).

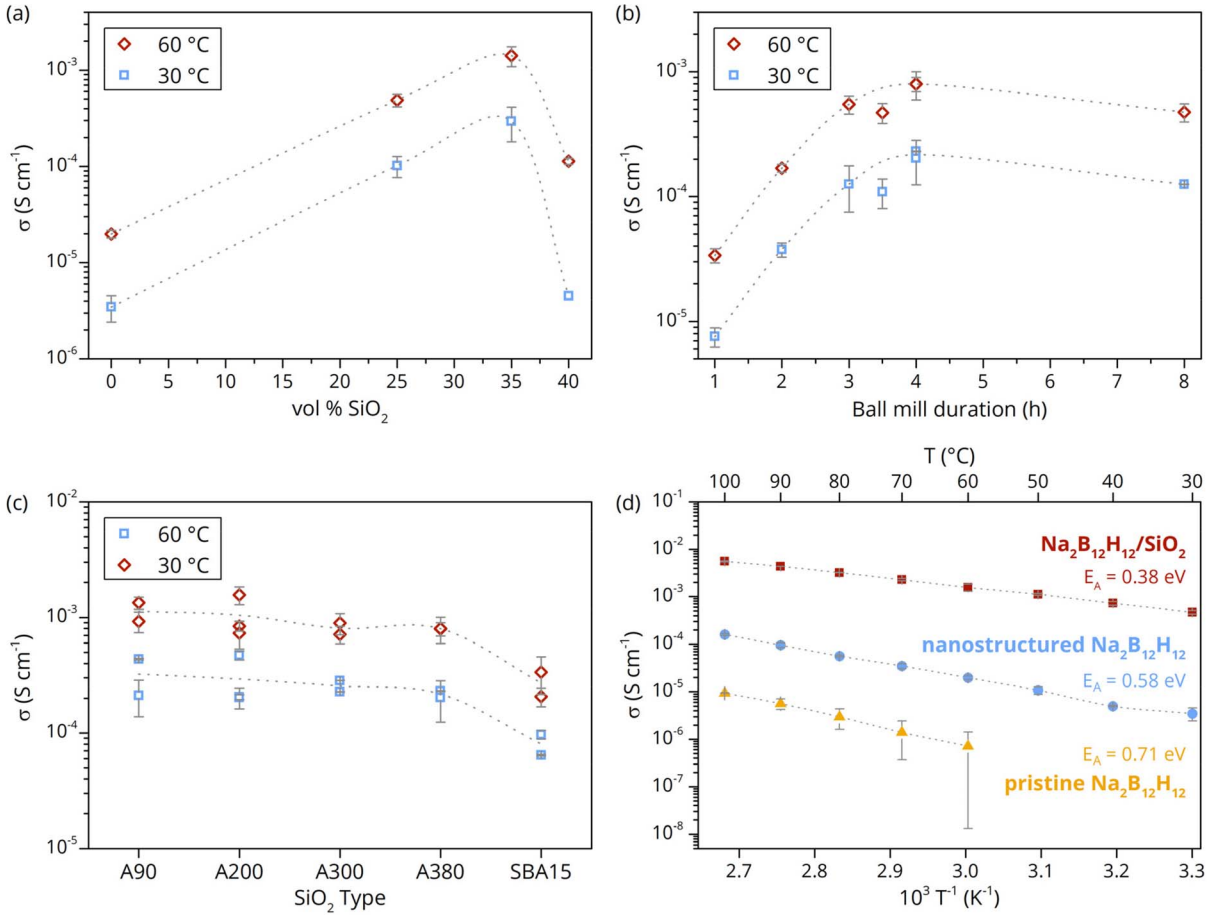

Fig. 2 Mean ionic conductivity and standard deviation during heating/cooling to the target temperature of (a) nanocomposites containing $Na_2B_{12}H_{12}$ and varying proportions of SiO_2-A380, (b) $Na_2B_{12}H_{12}$ + 35 vol% SiO_2-A380 after various mechanochemical treatment durations; (c) $Na_2B_{12}H_{12}$ nanoconfined in various types of SiO_2 (35 vol%) after 4 h ball milling; (d) $Na_2B_{12}H_{12}$ + 35 vol% SiO_2-A200 after 4 h of ball milling compared with pristine and nanostructured $Na_2B_{12}H_{12}$. Dotted lines serve as a visual guide.

milling time was investigated. Fig. 2b shows the ionic conductivities at 60 °C of nanocomposites ball-milled for different durations. The conductivity increases with the duration of the mechanochemical treatment until 4 h, after which it decreases upon further milling. This is in line with the increasing proportion of the high-temperature phase with the milling time, as seen in Fig. 1. The slight decrease in conductivity after more than 4 h of ball milling, despite the increase in the concentration of the high-temperature $Na_2B_{12}H_{12}$ phase, could be due to the severe distortion of the structure, as previously reported for $NaCB_{11}H_{12}$.[19,20] This is also in line with the high degree of amorphization observed in the XRD pattern upon prolonged milling. Thus, while high defect concentrations improve ionic conductivity, too high defect concentrations are detrimental to the overall ionic motion.

Since the nanocomposites contain a significant proportion of SiO_2, and the increased ionic conductivity is related to an interaction with SiO_2, the influence of the SiO_2 morphologies on the conductivity enhancement was investigated by using different types of silica (Table 1). For this purpose, $Na_2B_{12}H_{12}$-based nanocomposites were prepared using either ordered mesoporous SiO_2 (SBA-15) with a high surface area (800 $m^2\ g^{-1}$) or various amorphous pyrogenic silicas with surface areas ranging from 70 to 350 $m^2\ g^{-1}$. While the ionic conductivity of the nanocomposites with incorporated fumed silica showed only minor surface area dependency, the high surface area and different morphology of the ordered mesoporous silica seemed to have a negative impact (Fig. 2c). This is surprising because the ionic conductivity is expected to scale with the surface area of the nanocomposite, since the conductivity enhancement is related to interactions at the interface. This suggests that the interparticle pore volume between the nanosized primary fumed silica particles is advantageous for the mechanochemical synthesis approach, rather than the well-defined and narrow internal mesopores of SBA-15, which could be partly inaccessible, resulting in a higher void fraction and increased impedance. Indeed, SEM-EDS imaging and elemental mapping revealed a heterogeneous appearance independent of the silica type, whereby different sample domains were observed (Fig. S3 and S4). The microscopy images indicate that SiO_2 aggregates are partly embedded in $Na_2B_{12}H_{12}$, whereas bigger silica agglomerates are covered with $Na_2B_{12}H_{12}$. The irregular mixing

(heterogeneity) on the micrometer scale is consistent with the results of the conductivity measurements, which implies that the internal mesopores of SBA-15 cannot be completely filled *via* the mechanochemical nanocomposite preparation approach.

Based on the results discussed above, the use of 35 vol% SiO_2-A200 and the 4 h mechanochemical treatment gives rise to nanocomposites with the best ionic conductivity. Fig. 2d illustrates the ionic conductivity of $Na_2B_{12}H_{12}$ + 35 vol% SiO_2-A200 at various temperatures compared to the pristine (or bulk-like) and mechanochemically processed $Na_2B_{12}H_{12}$. The remarkable ~3 orders of magnitude increased ionic conductivity in the nanocomposite is mostly due to the reduction of the activation energy for Na-ion hopping from 0.71 eV (pristine $Na_2B_{12}H_{12}$) to 0.58 eV and 0.38 eV for the ball-milled (nanostructured) $Na_2B_{12}H_{12}$ and $Na_2B_{12}H_{12}/SiO_2$ nanocomposite, respectively. It is also clear that only nanostructuring of $Na_2B_{12}H_{12}$ already improves the ionic conductivity (1.9×10^{-5} S cm^{-1} at 60 °C) and reduces the activation energy for an ion-jump. Nevertheless, the presence of silica promotes the stabilization of the high-temperature polymorph, hence further facilitating the ionic motion and reducing the activation energy. This suggests that the addition of silica not only increases the concentration of the mobile ion carrier but also modifies the conduction mechanism, possibly originating from a chemically altered $Na_2B_{12}H_{12}$ interphase compound that forms at the interface with the oxide-containing framework, as reported for $Li_2B_{12}H_{12}$ and $LiBH_4$.[30,37] This will be discussed in detail in the next section.

Origin of the enhanced ionic conductivity in nanocomposites

Vibrational spectroscopy is a good approach to investigate the origin of the enhanced ionic conductivity by probing the surface chemistry and the nature of bonds in the pristine compounds and the nanocomposites. Fig. 3 shows the diffuse reflectance infrared spectroscopy data of the investigated nanocomposites compared to their physical mixtures. The surface chemistry of a dried SiO_2 framework is mainly dominated by absorption bands of isolated silanol groups (Si–OH) at 3750 cm^{-1} and features originating from inert siloxane groups (Si–O–Si) at low wavenumbers.[38] The absence of the O–H bending mode at ~1630 cm^{-1} and the overall weak intensity in the O–H vibration region (3300–3700 cm^{-1}) in the infrared spectra of the physical mixtures before the mechanochemical treatment indicate effective water removal during the drying step of the SiO_2, and a low degree of surface hydroxylation (Fig. 3a). The band assigned to free silanol groups is present in all physical mixtures, whereby the intensity scales with the surface area of the SiO_2 scaffold, but vanishes in the associated nanocomposites. Conversely, several overlapping bands emerge in the O–H stretch vibration region of the nanocomposite spectra, and their intensities are proportional to the presence of free silanol groups in the corresponding physical mixtures (Fig. 3b). The observed disappearance of the silanol groups upon nanocomposite formation is consistent with previous studies.[39,40] A plausible explanation would be that free silanol groups are reduced, *i.e.* to Si–H,[41] or lose their freedom to move in the solid. In this process, the $B_{12}H_{12}^{2-}$ anion could function as the reducing agent, hence being oxidized under the harsh synthesis conditions, and H_2O may be formed, as suggested by the presence of the O–H bending and stretching modes.

Further, all spectra in Fig. 3a contain the characteristic B–H vibration band of $Na_2B_{12}H_{12}$ at ~2500 cm^{-1}.[42] Noticeably, this peak is triple degenerate in the physical mixtures, whereas it has merged into a single broad feature for nanocomposites, indicating a distortion in the local chemical symmetry of the icosahedral boron cluster. Moreover, the shape of the asymmetric silanol bending mode at ~1080 cm^{-1}, slightly changed upon ball milling for all investigated samples. However, our results indicate that the quantity of free silanol groups prior to ball milling does not significantly affect the ionic conductivity; instead, the morphology of the framework plays a key role.

X-ray Raman scattering was employed to obtain further insight into the electronic structure of the nanocomposite and thus the conductivity enhancement mechanism. XRS experiments operated in the dipole limit allow for the investigation of light element K-edges, whereby results similar to XAS can be obtained. The advantage of XRS compared to XAS lies in its bulk sensitivity and the facilitated sample preparation, as the use of hard X-rays eliminates the need for measurements in high vacuum. Fig. 3c and d show the B and O K-edge spectra of $Na_2B_{12}H_{12}/SiO_2$ nanocomposites compared to reference compounds. The boron K-edge of the nanocomposite containing 35 vol% SiO_2 appears similar to that of the reference $Na_2B_{12}H_{12}$, since the overall signal is dominated by bulk-like $Na_2B_{12}H_{12}$ far from the interface with the SiO_2 (Fig. 3c). This is expected because the high fraction of $Na_2B_{12}H_{12}$ in the 35 vol% SiO_2 nanocomposite is essential to ensure a continuous Na-ion network in the SE, which is crucial for operation.

However, to exclusively probe the interphase layer a series of nanocomposites with higher SiO_2 contents (50 and 75 vol%), and hence lower bulk like $Na_2B_{12}H_{12}$, were investigated. Following this approach, only boron in close proximity to the oxidic scaffold material is probed, and changes can be unambiguously assigned to the interphase layer. Hence, the evolution of peak II, pronounced in the 50 and 75 vol% SiO_2 nanocomposites, is attributed to a mechanochemically formed interphase layer. This evidence is consistent with previous reports, describing the formation of a tertiary compound in $LiBH_4$ or $Li_2B_{12}H_{12}$-based nanocomposites.[29,35,43,44] Since a feature at 194 eV is characteristic for boron compounds with a trigonal planar geometry, such as found in $Na_2B_4O_7$ or B_2O_3, the increasing peak intensity at 194 eV in the investigated nanocomposites implies similar moieties are formed during an interface reaction between $Na_2B_{12}H_{12}$ and SiO_2 (Fig. 3c).[45–47]

Furthermore, the plateau ranging from peak III to peak V in pristine $Na_2B_{12}H_{12}$ flattens significantly in the nanocomposite samples, implying that the boron bonds of the interphase compound are still influenced by sodium, as can be seen in comparison to the reference spectra of $Na_2B_4O_7$.

Moreover, examination of the oxygen K-edge indicated peak-shape variations depending on the oxidic scaffold fraction. When high SiO_2 contents were used, an increasing influence of a feature at 535 eV is observed, which is associated with non-bridging oxygens (Fig. 3d).[48] This suggests that nonbridging

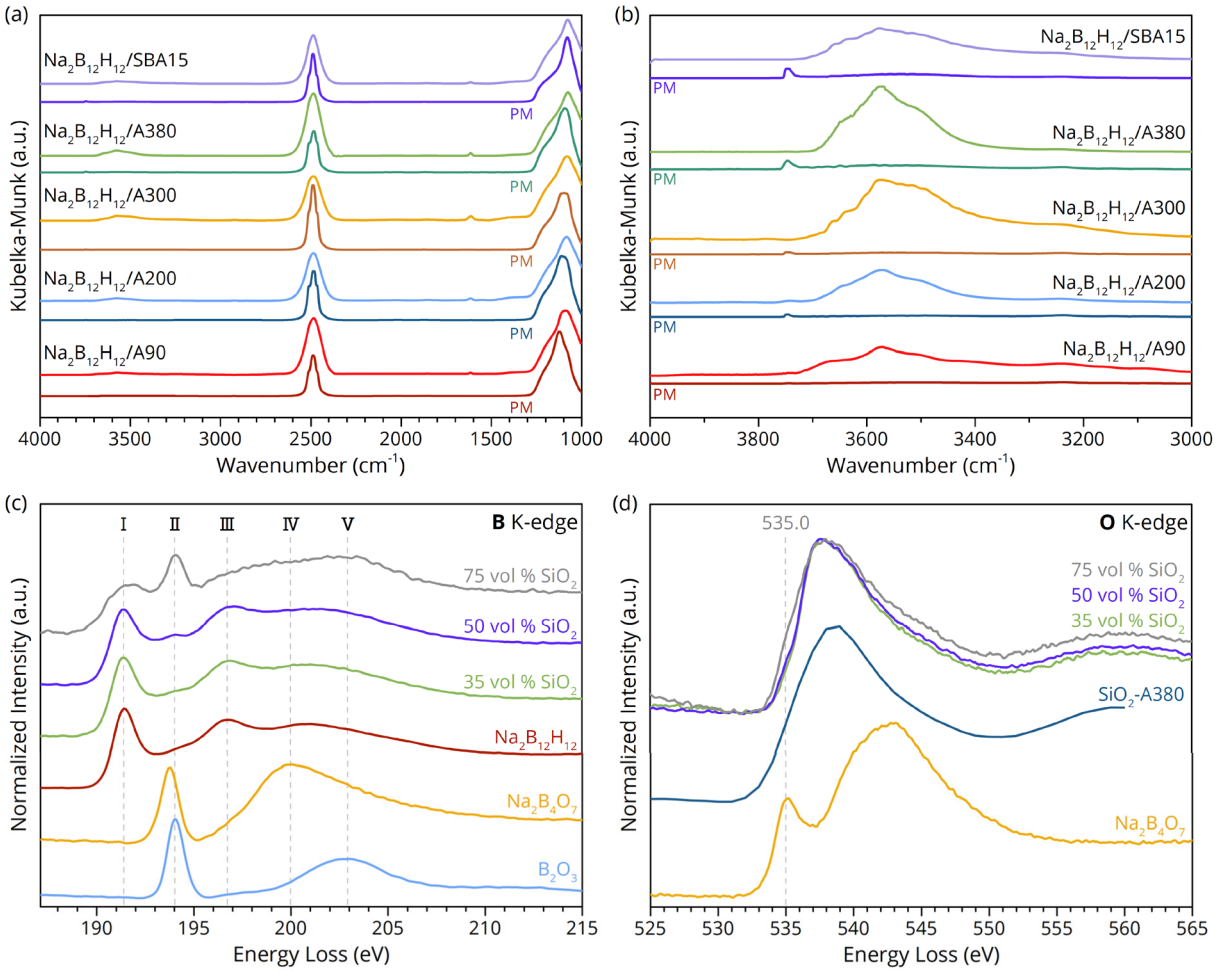

Fig. 3 (a) Diffuse reflectance infrared spectroscopy data of $Na_2B_{12}H_{12}$ + 35 vol% SiO_2 nanocomposites with different scaffold morphologies compared with the corresponding physical mixtures (PM) before ball milling; (b) zoomed region. (c) Boron and (d) oxygen K-edge XRS spectra of $Na_2B_{12}H_{12}$-based nanocomposites, containing various amounts of pyrogenic SiO_2 and reference compounds.

oxygen atoms react during the mechanochemical synthesis, which is in excellent agreement with the observed disappearance of the free silanol groups with DRIFTS.

Likewise, the Na K-edges were investigated and are given in Fig. S5. The edge-start of the $Na_2B_{12}H_{12}$ reference has a peak maximum at 1073.8 eV with a shoulder located at 1073.2 eV. However, for the nanocomposites, the edge-start maximum clearly shifted towards a lower energy loss of 1073.4 eV. Moreover, the main-edge feature of the reference material at 1075.8 eV is becoming less pronounced in favor of a peak evolution at 1076.6 eV and 1080.5 eV. This suggests that the sodium ions are located in structurally disordered environments, such as in sodium silicate glasses, where Na-ions are present as only weakly bound network modifiers.[49]

Since distinct changes in the boron, oxygen and sodium K-edge structure imply a chemical modification of $B_{12}H_{12}^{2-}$ following the mechanochemical treatment, the elemental distribution at the $Na_2B_{12}H_{12}/SiO_2$ interface was mapped with STEM-EDS (Fig. 4a–d and S6). The obtained images illustrate nano proximity between the constituent compounds. However, a boron enrichment at the surface of the SiO_2 agglomerate was observed, whereas sodium seems to be homogenously distributed over the SiO_2 particle (Fig. S7). The uneven boron distribution suggests the formation of an interphase layer anchored on the surface of silica particles. This is in excellent agreement with the disappearance of the free silanol groups, which are mainly located at the surface of SiO_2, pointing to a chemical reaction/interface formation with $Na_2B_{12}H_{12}$, where B–O bonds are formed at the interface.

The boron electronic structure was further investigated utilizing the spatial resolution of STEM-EELS, which enables zooming in closer to the interface (Fig. 4e). Details about the EELS background removal are given in Fig. S8. The STEM-EELS investigation suggests a modification of the $B_{12}H_{12}^{2-}$ anion in the nano proximity to the oxidic scaffold, which is consistent with the peak evolution at 194 eV observed with XRS measurements. However, the B K-edge structure in the vicinity of SiO_2 particles shows minor deviations from the XRS spectra obtained for pristine $Na_2B_{12}H_{12}$ (Fig. 3c), which can be attributed to plasmonic effects, the smaller sampling region, and the presence of small primary SiO_2 particles visible as bright unfocused spots on the TEM grid in Fig. 4d.

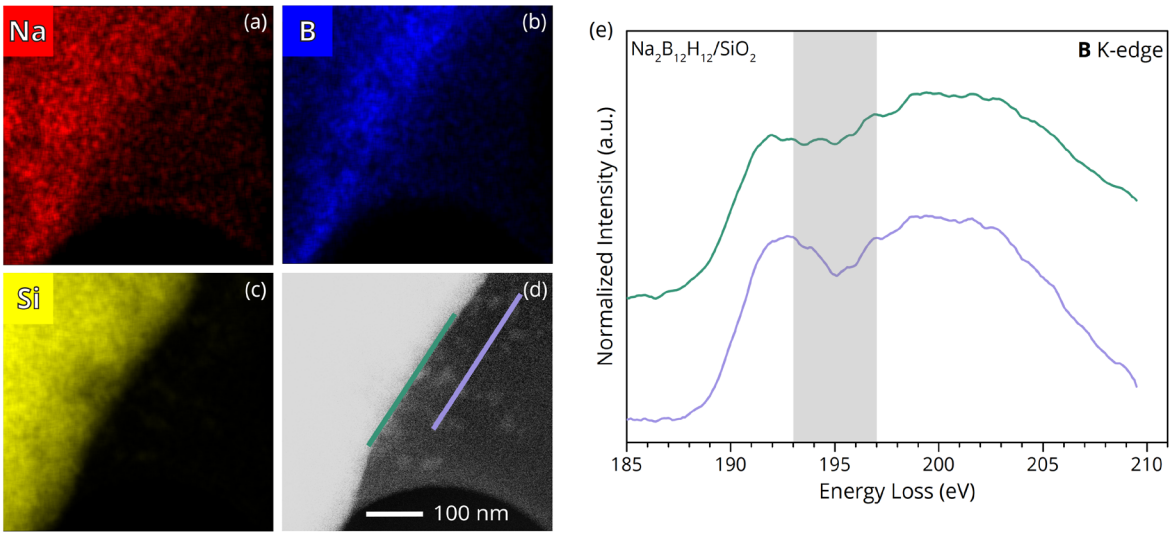

Fig. 4 Elemental distribution maps within $Na_2B_{12}H_{12}$ + 35 vol% SiO_2 recorded with energy dispersive X-ray spectroscopy of (a) sodium, (b) boron and (c) silicon. (d) Corresponding scanning transmission electron microscopy image. (e) Electron energy loss spectroscopy data of the indicated regions.

Nevertheless, both the XRS and the STEM-EELS results reveal modifications of the electronic structure of the $Na_2B_{12}H_{12}$ upon nanocomposite formation, whereby the B and Na (also O from the scaffold) are significantly altered at the interface. Together with the new vibrational modes and the disappearance of the oxide surface groups observed from the DRIFTS measurements, the existence of a boron-oxygen-rich, highly defective interphase at the $Na_2B_{12}H_{12}/SiO_2$ interface is highly likely.

Electrochemical properties and battery performance of the nanocomposites

In view of the good ionic conductivity of the samples, the electrochemical properties and performance of the material as SE in batteries were investigated. The EIS and chronoamperometry results in Fig. S9 and S10 indicate that the measured conductivity is truly ionic in nature; hence, the nanocomposites might be suitable as SEs. Specifically, the Na-ion transference number was estimated in a symmetric cell configuration with non-blocking Na metal electrodes to be t_{Na^+} = 0.97. The assigned value is in accordance with earlier reports,[25] although the additional polarization impedance is less pronounced (Fig. S11). To evaluate the oxidative electrochemical stability limit and compatibility with the highly reducing Na metal anode, linear sweep voltammetry was conducted (Fig. S12). An oxidative event with an onset voltage of E_{onset} = 3.9 V *vs.* Na^+/Na was found. Therefore, the oxidative stability limit is comparable to the value found for pristine $Na_2B_{12}H_{12}$. EIS performed before and after the electrochemically induced oxidative event clearly illustrates an increase in impedance, suggesting a partial decomposition of the material (Fig. S13), possibly to larger B_xH_y clusters as has been recently suggested computationally.[50] It is worth mentioning that the oxidative stability of $Na_2B_{12}H_{12}/SiO_2$ is enhanced compared to $Li_2B_{12}H_{12}$-based nanocomposites, which builds on previous findings regarding related hydridoborates.[29,30,51] The Na metal compatibility was tested in a symmetric cell configuration and exhibited stable polarization voltages for over 150 h, while alternating constant currents of 0.05 mA cm^{-2} were applied, which is in agreement with previous reports (Fig. S14).[25] Furthermore, critical current density measurements, utilizing the various fumed silica scaffolds with high or lower surface area, showed a similar current density limit of 0.3 mA cm^{-2} (Fig. S15).

Given the high oxidative stability and compatibility with Na metal, ASSBs based on $Na_2B_{12}H_{12}/SiO_2$ as SE were assembled in combination with a Na metal anode and PW ($Na_2Mn[Fe(CN)_6]$) or TiS_2 as active cathode material. Cells were operated at different temperatures ranging from RT (~20 °C) to 60 °C. The sodium manganese hexacyanoferrate cathode cell operated at 40 °C and C/10 showed nominal capacity fading during the first 10 cycles (Fig. 5a and b) before stabilizing at ~85% with respect to the first discharge capacity. The coulombic efficiency gradually increased with the number of cycles, from an average of 98.7% for cycles 7–10 to 99.7% for cycles 46–50. EIS measurements were performed periodically (Fig. S16) resulting in reduced coulombic efficiency values in the subsequent cycle. In addition, a battery cell with TiS_2 as cathode active material was operated at 60 °C, demonstrating the versatile suitability of the developed nanocomposite SE for a wide temperature range (Fig. S17).

The charge–discharge profile of the PW-ASSB operated at RT and C/20 is shown in Fig. 5c and d. It can be seen that the investigated $Na_2B_{12}H_{12}/SiO_2$ nanocomposite exhibits excellent properties as an SE, which is reflected in overall high coulombic efficiency values. Furthermore, a capacity retention of 96.9% was measured after 50 cycles, while fluctuations in room temperature are likely responsible for the recovery from 94.7% capacity retention after the 45th cycle. Nevertheless, the overall

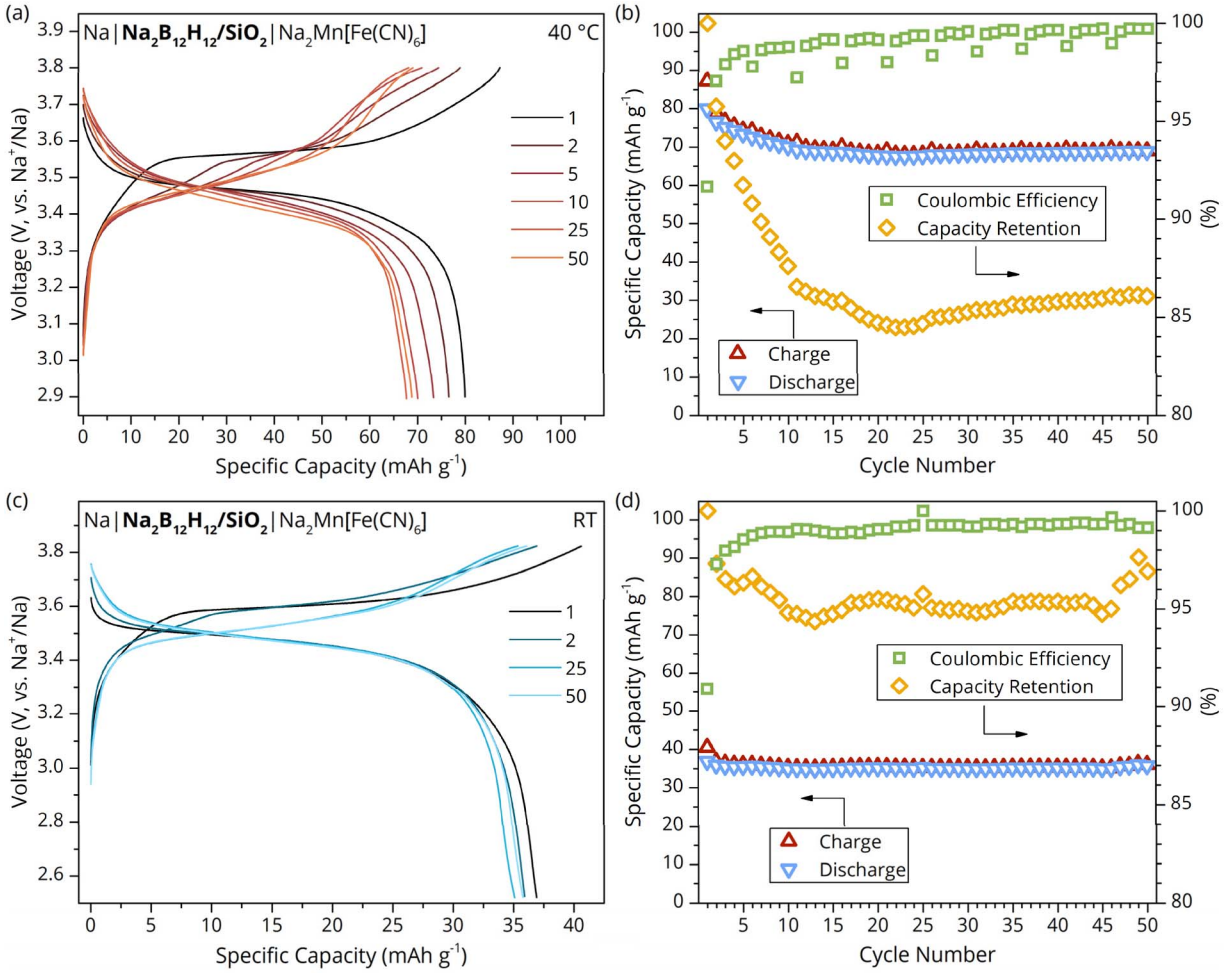

Fig. 5 Battery performance of all-solid-state batteries ($Na|Na_2B_{12}H_{12}/SiO_2|Na_2Mn[Fe(CN)_6]$). (a) Cycling profile and (b) details about coulombic efficiency and capacity retention at 40 °C and C/10 (50.51 μA cm^{-2}). (c) Cycling profile and (b) cycling performance at room temperature and C/20 (27.1 μA cm^{-2}).

measured specific capacity is low compared to a PW-ASSB cell operated at 40 °C. The reduced capacity is attributed to increased internal impedance and lower electrotonic conductivity of PW in the cathode composite in a colder environment.[52] Furthermore, an uneven distribution of electronically conductive carbon in the cathode composite mixture may have resulted in electronically isolated PW grains that consequently remain electrochemically inactive during battery cycling. While the cathode formulation requires further improvement to increase the charge/discharge capacity, this work clearly demonstrates the compatibility of $Na_2B_{12}H_{12}/SiO_2$ with Na metal anode and state-of-the-art high-voltage cathode materials (PW) at ambient conditions.

Conclusions

We have studied the effects of SiO_2 on the ionic conductivity and electrochemical properties of $Na_2B_{12}H_{12}$ in all-solid-state sodium batteries. Our work revealed that $Na_2B_{12}H_{12}/SiO_2$ nanocomposites exhibit more than 3 and 2 orders of magnitude higher ionic conductivity at room temperature compared to the pristine and ball-milled $Na_2B_{12}H_{12}$, respectively. Structural and electronic characterization suggest that the enhanced ionic conductivity is related to interface reactions with surface groups of the SiO_2 scaffold, leading to highly disordered $Na_2B_{12}H_{12}$ with partially oxidized $B_{12}H_{12}^{2-}$. The morphology of the SiO_2 scaffolds and preparation conditions for the nanocomposite were found to influence the ionic conductivity. Moreover, upon addition of SiO_2, the electrochemical oxidative stability was retained at 3.9 V *vs.* Na^+/Na. This results in a good cycling stability in combination with Na metal anode and both TiS_2 and Prussian white cathodes between room temperature and 60 °C. Our work clearly demonstrates the efficacy of interface engineering in improving the ionic conductivity and electrochemical properties of sodium-based solid electrolytes, and their appealing properties for application in high-capacity all-solid-state sodium batteries.

Author contributions

J. D. H. and P. N. conceived the experiments. J. D. H. and G. M. synthesized the samples, carried out electrochemical and

structural measurements, and analyzed the data. J. D. H., M. L., J. C. V., M. S. and H. G. performed the XRS measurements. S. J. T. carried out the TEM-EELS measurements, and K. K. acquired the SEM images. J. D. H. and P. N. wrote the original manuscript. F. M., P. E. d. J. and P. N. supervised the research and reviewed the manuscript.

Conflicts of interest

The authors declare no competing financial interest.

Data availability

The data underlying this study are available at the Zenodo repository at: https://doi.org/10.5281/zenodo.17378151.

Supplementary information (SI): additional structural, electronic, and electrochemical characterizations. See DOI: https://doi.org/10.1039/d5ta09128d.

Acknowledgements

Ramon van Maanen, Jan Willem de Rijk and Dennie Wezendonk are thanked for their technical assistance. The authors acknowledge the financial support from the Dutch Research Council (NWO). This publication is part of the 'BatteryNL – Next Generation Batteries based on Understanding Materials Interfaces' project (with project number NWA.1389.20.089) of the NWA research programme 'Research on Routes by Consortia (ORC)' funded by NWO. We acknowledge DESY (Hamburg, Germany), a member of the Helmholtz Association HGF, for the provision of experimental facilities and beamline P01, PETRA III. Beamtime was allocated for proposal I-20241256. PN and ML acknowledge funding from the European Union under the ERC Grant agreement no. 101171583 – Interfacial Ionics. For access to the TFS Spectra300 microscope at EM Centre Utrecht, we acknowledge the Netherlands Electron Microscopy Infrastructure (NEMI), project number 184.034.014, part of the National Roadmap and financed by NWO. GM and FM acknowledge funding from the European Union under the MSCA-IF Grant agreement no. 101069033 – STREAM and Next Generation EU, and the program DM 737/2021 fundings 2021–2022. Views and opinions expressed are, however, those of the author(s) only and do not necessarily reflect those of the European Union or the European Research Council Executive Agency (granting authority). Neither the European Union nor the granting authority can be held responsible for them.

References

1 D. M. Davies, M. G. Verde, O. Mnyshenko, Y. R. Chen, R. Rajeev, Y. S. Meng and G. Elliott, *Nat. Energy*, 2019, **4**, 42–50.
2 F. Duffner, N. Kronemeyer, J. Tübke, J. Leker, M. Winter and R. Schmuch, *Nat. Energy*, 2021, **6**, 123–134.
3 P. K. Nayak, L. Yang, W. Brehm and P. Adelhelm, *Angew. Chem., Int. Ed.*, 2018, **57**, 102–120.
4 K. M. Abraham, *ACS Energy Lett.*, 2020, **5**, 3544–3547.
5 C. Bai, Y. Li, G. Xiao, J. Chen, S. Tan, P. Shi, T. Hou, M. Liu, Y.-B. He and F. Kang, *Chem. Rev.*, 2025, **125**, 6541–6608.
6 S. Chen, C. Wu, L. Shen, C. Zhu, Y. Huang, K. Xi, J. Maier and Y. Yu, *Adv. Mater.*, 2017, **29**, 1700431.
7 C. Zhao, L. Liu, X. Qi, Y. Lu, F. Wu, J. Zhao, Y. Yu, Y.-S. Hu and L. Chen, *Adv. Energy Mater.*, 2018, **8**, 1703012.
8 Y. Yung-Fang Yu and J. T. Kummer, *J. Inorg. Nucl. Chem.*, 1967, **29**, 2453–2475.
9 A. Hayashi, K. Noi, A. Sakuda and M. Tatsumisago, *Nat. Commun.*, 2012, **3**, 856.
10 Z. Lu, J.-X. Kang, P. Qiu and X. Chen, *Batter. Supercaps*, 2025, **8**, e202400636.
11 M. Jin, D. Xu, Z. Su, R. Liu, M. Xiang, Y. Cheng, R. Wu and Y. Guo, *Adv. Mater.*, 2025, e07809.
12 F. Cuevas, M. B. Amdisen, M. Baricco, C. E. Buckley, Y. W. Cho, P. de Jongh, L. M. de Kort, J. B. Grinderslev, V. Gulino, B. C. Hauback, M. Heere, T. Humphries, T. R. Jensen, S. Kim, K. Kisu, Y.-S. Lee, H.-W. Li, R. Mohtadi, K. T. Møller, P. Ngene, D. Noréus, S.-I. Orimo, M. Paskevicius, M. Polanski, S. Sartori, L. N. Skov, M. H. Sørby, B. C. Wood, V. A. Yartys, M. Zhu and M. Latroche, *Prog. Energy*, 2022, **4**, 032001.
13 J. Janek and W. G. Zeier, *Nat. Energy*, 2023, **8**, 230–240.
14 L. M. de Kort, V. Gulino, P. E. de Jongh and P. Ngene, *J. Alloys Compd.*, 2022, **901**, 163474.
15 Q. Liu, X. Zhao, Q. Yang, L. Hou, D. Mu, G. Tan, L. Li, R. Chen and F. Wu, *Adv. Mater. Technol.*, 2023, **8**, 2200822.
16 T.-T. Le, M. Abbas, D. M. Dreistadt, T. Klassen and C. Pistidda, *Chem. Eng. J.*, 2023, **473**, 145315.
17 W. S. Tang, M. Matsuo, H. Wu, V. Stavila, A. Unemoto, S.-I. Orimo and T. J. Udovic, *Energy Storage Mater.*, 2016, **4**, 79–83.
18 T. J. Udovic, M. Matsuo, A. Unemoto, N. Verdal, V. Stavila, A. V. Skripov, J. J. Rush, H. Takamura and S.-I. Orimo, *Chem. Commun.*, 2014, **50**, 3750–3752.
19 V. Gulino, A. Longo, L. M. de Kort, H. P. Rodenburg, F. Murgia, M. Brighi, R. Černý, C. J. Sahle, M. Sundermann, H. Gretarsson, F. de Groot and P. Ngene, *Small Methods*, 2024, **8**, 2300833.
20 F. Murgia, M. Brighi, L. Piveteau, C. E. Avalos, V. Gulino, M. C. Nierstenhöfer, P. Ngene, P. de Jongh and R. Černý, *ACS Appl. Mater. Interfaces*, 2021, **13**, 61346–61356.
21 M. Brighi, F. Murgia, Z. Łodziana, P. Schouwink, A. Wołczyk and R. Cerny, *J. Power Sources*, 2018, **404**, 7–12.
22 M. Brighi, F. Murgia and R. Černý, *Cell Rep. Phys. Sci.*, 2020, **1**, 100217.
23 K. Yoshida, T. Sato, A. Unemoto, M. Matsuo, T. Ikeshoji, T. J. Udovic and S.-I. Orimo, *Appl. Phys. Lett.*, 2017, **110**, 103901.
24 X. Luo, A. Rawal and K.-F. Aguey-Zinsou, *Inorganics*, 2021, **9**, 2.
25 Z. Su, M. Jin, C. Hu, R. Liu, R. Wu, D. Xu and Y. Guo, *ACS Appl. Energy Mater.*, 2025, **8**, 5656–5663.
26 X. Luo, A. Rawal and K.-F. Aguey-Zinsou, *J. Phys. Chem. C*, 2024, **128**, 14861–14870.
27 M. S. Andersson, V. Stavila, A. V. Skripov, M. Dimitrievska, M. T. Psurek, J. B. Leão, O. A. Babanova, R. V. Skoryunov,

A. V. Soloninin, M. Karlsson and T. J. Udovic, *J. Phys. Chem. C*, 2021, **125**, 16689–16699.
28 Y. Dou, H. A. Hansen, S.-M. Xu and D. Blanchard, *Mater. Chem. Front.*, 2021, **5**, 4989–4996.
29 C. Zhou, H. Sun, Q. Wang, J. B. Grinderslev, D. Liu, Y. Yan and T. R. Jensen, *J. Alloys Compd.*, 2023, **938**, 168689.
30 J. D. Hehn, H. P. Rodenburg, M. Lazemi, J. C. Verschoor, M. Perxés Perich, M. Sundermann, H. Gretarsson, J. E. S. van der Hoeven, F. M. F. de Groot, P. E. de Jongh and P. Ngene, *ACS Appl. Mater. Interfaces*, 2025, **17**, 33824–33833.
31 S. Das, P. Ngene, P. Norby, T. Vegge, P. E. de Jongh and D. Blanchard, *J. Electrochem. Soc.*, 2016, **163**, A2029.
32 M. H. W. Verkuijlen, P. Ngene, D. W. de Kort, C. Barré, A. Nale, E. R. H. van Eck, P. J. M. van Bentum, P. E. de Jongh and A. P. M. Kentgens, *J. Phys. Chem. C*, 2012, **116**, 22169–22178.
33 L. M. de Kort, O. E. Brandt Corstius, V. Gulino, A. Gurinov, M. Baldus and P. Ngene, *Adv. Funct. Mater.*, 2023, **33**, 2209122.
34 S. Brunauer, P. H. Emmett and E. Teller, *J. Am. Chem. Soc.*, 1938, **60**, 309–319.
35 L. M. de Kort, M. Lazemi, A. Longo, V. Gulino, H. P. Rodenburg, D. Blanchard, C. Sahle, M. Sundermann, H. Gretarsson, A. M. J. van der Eerden, H. Elnaggar, F. M. F. de Groot and P. Ngene, *Adv. Energy Mater.*, 2024, **14**, 2303381.
36 N. Verdal, J.-H. Her, V. Stavila, A. V. Soloninin, O. A. Babanova, A. V. Skripov, T. J. Udovic and J. J. Rush, *J. Solid State Chem.*, 2014, **212**, 81–91.
37 V. Gulino, L. Barberis, P. Ngene, M. Baricco and P. E. de Jongh, *ACS Appl. Energy Mater.*, 2020, **3**, 4941–4948.
38 L. T. Zhuravlev, *Colloids Surf., A*, 2000, **173**, 1–38.
39 P. Ngene, S. F. H. Lambregts, D. Blanchard, T. Vegge, M. Sharma, H. Hagemann and P. E. de Jongh, *Phys. Chem. Chem. Phys.*, 2019, **21**, 22456–22466.
40 L. M. de Kort, J. Harmel, P. E. de Jongh and P. Ngene, *J. Mater. Chem. A*, 2020, **8**, 20687–20697.
41 S. F. H. Lambregts, L. M. de Kort, F. Winkelmann, M. Felderhoff, P. Ngene, E. R. H. van Eck and A. P. M. Kentgens, *J. Phys. Chem. C*, 2024, **128**, 12186–12193.
42 E. L. Muetterties, R. E. Merrifield, H. C. Miller, W. H. Knoth and J. R. Downing, *J. Am. Chem. Soc.*, 1962, **84**, 2506–2508.
43 P. S. Miedema, P. Ngene, A. M. J. van der Eerden, D. Sokaras, T.-C. Weng, D. Nordlund, Y. S. Au and F. M. F. de Groot, *Phys. Chem. Chem. Phys.*, 2014, **16**, 22651–22658.
44 Y. S. Choi, Y.-S. Lee, D.-J. Choi, K. H. Chae, K. H. Oh and Y. W. Cho, *J. Phys. Chem. C*, 2017, **121**, 26209–26215.
45 M. E. Fleet and S. Muthupari, *J. Non-Cryst. Solids*, 1999, **255**, 233–241.
46 M. E. Fleet and X. Liu, *Phys. Chem. Miner.*, 2001, **28**, 421–427.
47 G. S. Henderson, F. M. F. de Groot and B. J. A. Moulton, *Rev. Mineral. Geochem.*, 2014, **78**, 75–138.
48 F. Frati, M. O. J. Y. Hunault and F. M. F. de Groot, *Chem. Rev.*, 2020, **120**, 4056–4110.
49 S. De Wispelaere, D. Cabaret, C. Levelut, S. Rossano, A.-M. Flank, P. Parent and F. Farges, *Chem. Geol.*, 2004, **213**, 63–70.
50 R. Asakura, Z. Łodziana, R. Grissa, D. Rentsch, C. Battaglia and A. Remhof, *ACS Appl. Energy Mater.*, 2025, **8**, 9637–9645.
51 O. Tutusaus, H. Kuwata, M. J. Counihan and R. Mohtadi, *Chem. Commun.*, 2023, **59**, 4746–4749.
52 R. Sun and Y. You, *ACS Appl. Mater. Interfaces*, 2023, **15**, 44599–44606.